Research article

Sebastian Meyer*, Zhi Yang Tan and Dmitry N. Chigrin*

Multiphysics simulations of adaptive metasurfaces at the meta-atom length scale

https://doi.org/10.1515/nanoph-2019-0458
Received November 5, 2019; revised December 17, 2019; accepted January 5, 2020

Abstract: Adaptive metasurfaces (MSs) provide immense control over the phase, amplitude and propagation direction of electromagnetic waves. Adopting phase-change materials (PCMs) as an adaptive medium allows us to tune functionality of MSs at the meta-atom length scale providing full control over MS (re-)programmability. Recent experimental progress in the local switching of PCM-based MSs promises to revolutionize adaptive photonics. Novel possibilities open new challenges, one of which is a necessity to understand and be able to predict the phase transition behavior at the sub-micrometer scale. A meta-atom can be switched by a local deposition of heat using optical or electrical pulses. The deposited energy is strongly inhomogeneous and the resulting phase transition is spatially non-uniform. The drastic change of the material properties during the phase transition leads to time-dependent changes in the absorption rate and heat conduction near the meta-atom. These necessitate a self-consistent treatment of electromagnetic, thermal and phase transition processes. Here, a self-consistent multiphysics description of an optically induced phase transition in MSs is reported. The developed model is used to analyze local tuning of a perfect absorber. A detailed understanding of the phase transition at the meta-atom length scale will enable a purposeful design of programmable adaptive MSs.

Keywords: phase change materials; multiphysics simulations; phase field model; active metamaterials; perfect absorber.

***Corresponding authors: Sebastian Meyer,** I. Physikalisches Institut (1A), RWTH Aachen University, Sommerfeldstraße 14, 52074 Aachen, Germany, e-mail: smeyer@physik.rwth-aachen.de. https://orcid.org/0000-0003-4208-0988; and
Dmitry N. Chigrin, I. Physikalisches Institut (1A), RWTH Aachen University, 52074 Aachen, Germany; and DWI – Leibniz Institute for Interactive Materials, 52074 Aachen, Germany, e-mail: chigrin@dwi.rwth-aachen.de. https://orcid.org/0000-0002-8197-707X
Zhi Yang Tan: I. Physikalisches Institut (1A), RWTH Aachen University, 52074 Aachen, Germany

1 Introduction

Metasurfaces (MSs) are quasi-two-dimensional arrangements of subwavelength-sized, resonant elements ("meta-atoms") [1, 2]. The functionality of MSs is provided through a combined response of these meta-atoms [3, 4]. Adjusting the resonant properties and the arrangement of meta-atoms allows us to design artificial thin-film materials, enabling unprecedented control over the phase, amplitude and direction of electromagnetic waves. Different physical mechanisms have been successfully employed to tune entire MSs, e.g. by altering the orientation order in liquid crystals [5–7], mechanically altering the MS [8, 9], altering the carrier concentration in graphene [10, 11], transparent conductive oxides [12] and doped semiconductors [13] and by inducing a volatile phase transition in vanadium dioxide [14]. The ability to alter the optical properties of *individual meta-atoms* by external stimuli in a post-production step opens up an avenue towards adaptive MSs with freely (re-)programmable optical properties [15, 16]. However, due to the volatile and/or nonlocal nature of the tuning mechanisms, the above-mentioned materials cannot be easily used for this purpose. Adopting phase-change materials (PCMs) as an adaptive medium enables the tuning of MSs at the meta-atom length scale. PCMs possess at least two thermodynamically (meta-) stable states (amorphous and crystalline) with drastically different physical properties which makes them a highly suited material for optical, electric data storage [17] and neuromorphic computing [18]. A typical change of the real part of the refractive index upon the phase transition can be as high as $n_A = 3.0$ to $n_C = 6.0$ in the mid-infrared spectral range [19]. The phase transition is nonvolatile and reversible [20]. These properties make PCMs an ideal choice for adaptive MSs. PCMs have been successfully employed in different MS-based applications [21–24]. Switching is achieved by inducing a phase transition in the entire MSs by heating [25], and short electrical [26] or optical pulses [27]. While a typical PCM possesses considerable optical loss at the near-infrared and optical frequencies, most of the reported applications are in the mid-infrared spectral range. However, this limitation can be circumvented by

employing emerging PCMs with lower optical losses in this spectral range [28].

Recently, it has been demonstrated that addressing and tuning the resonant properties of individual meta-atoms of infrared MSs is possible employing focused visible light [29]. The same technique has been utilized to fabricate dielectric infrared MSs [30, 31]. The optically induced phase transition takes place in a sub-micrometer-sized volume at a sub-microsecond time scale. It is driven by local energy deposition. Due to the non-stationary nature of the switching process and the complex geometry of the meta-atom, the deposited energy is strongly inhomogeneous and the resulting phase transition is spatially non-uniform [29]. The drastic change of the material properties during the phase transition further leads to spatially inhomogeneous, time-dependent changes in the absorption rate and heat conduction near the meta-atom. In order to be able to interpret and predict the optical response of the PCM-based MSs, a self-consistent treatment of light propagation and absorption, transient heat transfer and phase transition kinetics at a sub-micrometer length scale is required. A naive approach assuming a simple geometry of a crystallized region does not suffice to understand observed changes of the resonant response of a locally tuned MS [29].

Different approaches to simulate the phase transition in PCMs are available, ranging in complexity from ab initio to effective medium models. Ab initio [32] simulations at a molecular length scale can provide the most detailed information on phase transition kinetics at a price of high computational cost. These methods, though powerful, are unrealistic to use at the length scale of one or a few meta-atoms. Effective medium methods, like the widely used Johnson-Mehl-Avrami-Kolmogorov (JMAK) [33–37] model, are computationally very efficient. Unfortunately, they rely on volumetric averaging procedures and are applicable for volumes much larger than the characteristic volume of the individual crystallite. This requirement is hardly met at typical meta-atom dimensions. There are a number of methods providing better trade-offs between details of the phase transition kinetics and the computational costs. The most common examples are rate equations [38], Cellular Automata [39] and phase field [40–42] methods. Among those models, the phase field model provides an optimal balance between physical details and computational costs.

Here, we present a self-consistent multiphysics description of optically induced non-stationary and spatially inhomogeneous crystallization of PCMs in infrared MSs based on a phase field model of phase transition kinetics. We apply the developed model to analyze the local tuning of a thin-film MS perfect absorber and demonstrate that a self-consistent multiphysics description is necessary in order to accurately describe the perfect absorber behavior. The developed model provides a better understanding of the phase transition at the meta-atom length scale and will enable and facilitate a more purposeful designing of programmable adaptive MSs.

2 Results and discussion

2.1 Crystallization kinetics model

The phase field model is a phenomenological approach to simulate phase transitions [43, 44]. The local crystallinity of the sample is represented by the non-conserved-order parameter ϕ, with $\phi = 0$ in the amorphous and $\phi = 1$ in the crystalline phase. An interface between two phases is a smooth transition and occupies some finite volume. The order parameter in the interface region assumes values between 0 and 1. The evolution of the order parameter is governed by the Allen-Cahn equation [45]:

$$\frac{\partial \phi}{\partial t} = -M_{\phi} \frac{\delta G}{\delta \phi}. \tag{1}$$

Here, t is the time, G is the total Gibbs free energy of the PCM and M_{ϕ} is the phase field mobility. $\frac{\delta G}{\delta \phi}$ represents the functional derivative of G with respect to ϕ. The Gibbs free energy is assumed to be [46]

$$G(\phi) = \int_V \mathrm{d}^3 x \left(g(\phi) + \frac{\epsilon^2}{2} (\nabla \phi)^2 \right), \tag{2}$$

with V being the volume of the system. The first term in the brackets is a bulk contribution to the free energy density and the second one is a contribution due to the interface between two phases. The parameter ε controls the width of the interface region. In order to account for a phase separation phenomenon, the bulk Gibbs free energy is given in the form of an asymmetric double-well potential

$$g(\phi) = W \phi^2 (1-\phi)^2 - \Delta G_V \phi^2 (3-2\phi) \tag{3}$$

with W and ΔG_V being the phenomenological parameters determining the absolute and the relative well depths, respectively.

After taking the functional derivative of (2) one arrives at the following form of the evolution equation for the order parameter:

$$\frac{\partial\phi}{\partial t} = -M_\phi(2W\phi(1-\phi)(1-2\phi) - 6\Delta G_V\phi(1-\phi) - \epsilon^2\nabla^2\phi). \quad (4)$$

Defining the interfacial energy γ, the interface thickness between two phases ζ and the growth velocity of the crystalline grain v_g, the remaining parameters can be expressed as

$$M_\phi = \frac{1}{6\zeta}\frac{v_g}{\Delta G_v},\ W = \frac{3\gamma}{\zeta},\ \epsilon = \sqrt{6\gamma\zeta}. \quad (5)$$

For the growth velocity, the Arrhenius [38] and the Frenkel models [47, 48] are used for temperatures below and above the glass transition temperature, respectively [for more details see Supporting Information (SI)]. The free energy density difference ΔG_V is given by the Thompson-Spaepen equation [49] (SI). The resulting equation (4) describes the evolution of the crystalline phase in time and space, but does not account for nucleation. Here, nucleation events are incorporated explicitly using the method described by Simmons et al. [50]. The nucleation rate is given by the classical nucleation theory expression [51, 52] (SI).

The evolution equation (4) is solved using the finite difference method with a 7-point stencil and the corrector-predictor scheme (SI) using the custom MATLAB code. At all PCM outer boundaries, a zero-flux boundary condition is used, i.e. $\mathbf{n}\cdot\nabla\phi = 0$. Here, $\mathbf{n}$ is an outer unit normal vector at the PCM boundary. All relevant parameters of the model are given in the SI. In order to test the reliability of the model, the crystallization kinetics of a thin film (85 nm) of $Ge_2Sb_2Te_5$ (GST) phase change material is simulated at a constant temperature ($T = 404$ K). Good agreement with experimental results [53] can be demonstrated (SI).

2.2 Perfect absorber

We further apply the phase field model of crystallization kinetics to analyze the laser-induced tuning of an MS perfect absorber [54]. The perfect absorber is chosen here as a simple example of an adaptive MS-based optical element. Inducing the same crystallization pattern near every meta-atom enables a post-production fine tuning of the absorption band spectral position, while inducing different crystallization patterns near a group of meta-atoms enables (re-)programming of both width and spectral position of the absorption band. Our perfect absorber model consists of an array (period 800 nm) of square aluminum nano-antennas (length 400 nm, thickness 35 nm) stacked above a dielectric buffer layer ($ZnS:SiO_2$, thickness 40 nm) followed by an aluminum mirror (thickness 100 nm) on a semi-infinite silicon substrate (see Figure 1A). The antenna array is covered with a GST layer (thickness 65 nm). On top of the GST layer, a 25-nm-thick silicon layer is placed to facilitate thermal management. Dielectric functions of all used materials are reported in the SI.

The perfect absorber is optimized for the mid-infrared spectral range and demonstrates near-perfect absorption at 2722 cm^{-1} and 2193 cm^{-1} for a GST layer in the amorphous and the crystalline state, respectively. A continuous tuning of the absorption band between two limiting states (fully amorphous and fully crystalline) can be achieved by locally crystallizing the GST near the antenna. If a crystallized volume in the form of an ideal cylinder with the height of the GST layer can be realized, the spectral position of the absorption band can be shifted by changing the diameter of the cylinder. This is illustrated in Figure 1B for different diameters of the perfectly crystallized volume. With increasing diameter the absorption peak is shifted to lower wavenumbers (Figure 1C) and covers the full

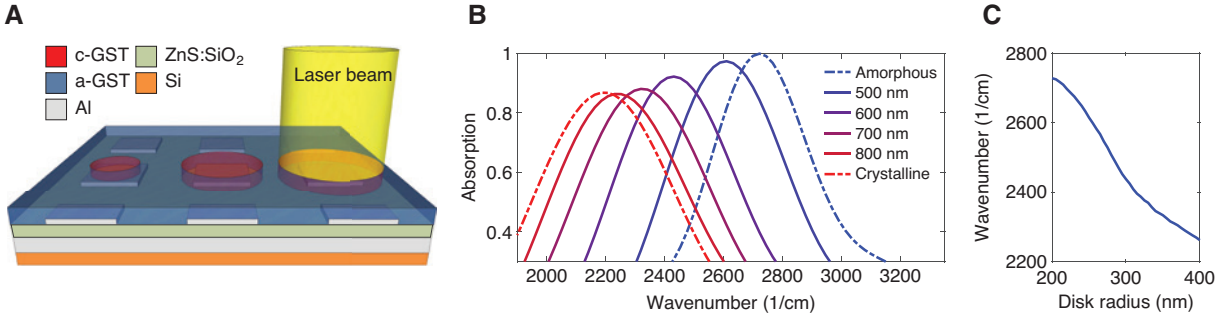

Figure 1: Switching scheme and idealized description of optical switching.
(A) A sketch of the studied MS perfect absorber. Different illumination conditions lead to crystallized volumes of variable sizes. The superstrate layer is not shown for clarity. (B) Absorption spectrum of the perfect absorber for a completely amorphous (blue) and crystalline (red) GST layer (dashed-dotted lines) and for idealized cylindrical crystallized volumes with diameters of 500 nm, 600 nm, 700 nm and 800 nm. (C) Position of the absorption maximum as a function of the switched cylinder radius.

tuning range of 529 cm^{-1}. The absorption spectra in the fully amorphous and fully crystalline states are shown in Figure 1B as dashed-dotted blue and red curves, respectively. The spectra are calculated using CST Studio Suite. A finite integration technique with a plane wave excitation has been used. Periodic and open boundary conditions have been employed in horizontal and vertical directions, respectively. Here, we assumed that every meta-atom is switched identically.

2.3 Laser-induced tuning

Local phase transition near an individual nano-antenna can be achieved by employing a focused laser beam [29]. We simulate the laser beam as a continuous wave Gaussian beam with a waist diameter of 800 nm, a wavelength of 405 nm (corresponds to the operation wavelength of the "Blu-Ray" laser diodes) and a power of 8.5 mW. The beam is focused on the center of a single nano-antenna. Optical absorption in the GST layer leads to heat accumulation, which provides the energy to drive local crystallization in the PCM layer. As both optical and thermal properties of the amorphous and the crystalline phases are drastically different [19, 55], electromagnetic, thermal and phase transition simulations have to be coupled self-consistently in order to adequately model non-stationary and spatially inhomogeneous crystallization near the nano-antenna.

First, the optical absorption at the wavelength of the switching laser is calculated. The absorbed power map is then used as a heat source in transient heat transfer simulations. Both types of simulations are performed in CST Studio Suite using a finite integration technique. The temperature map at a given time step is then used in the custom phase field model code to update the spatial distribution of the amorphous and the crystalline phases. The new phase distribution in the GST layer is imported back to the electromagnetic and thermal models and the simulation cycle is repeated. The numerical workflow is detailed in the SI. The surrounding temperature is assumed to be 293 K. In the electromagnetic and the heat transfer solvers, open boundary conditions are used in all spatial directions.

Results of the multiphysics simulations of the optical tuning of the MS perfect absorber are shown in Figure 2. Snapshots of the phase distribution in the GST layer after 100 ns, 250 ns and 1.5 µs are shown (Figure 2A). The unit cell is cut in half for clarity. It can be clearly seen that the shape of the crystallized volume is always far more complex than the simple circular cylinder approximation. After 100 ns, only a few unconnected nuclei above and next to the nano-antenna exist. Most of the nuclei form at

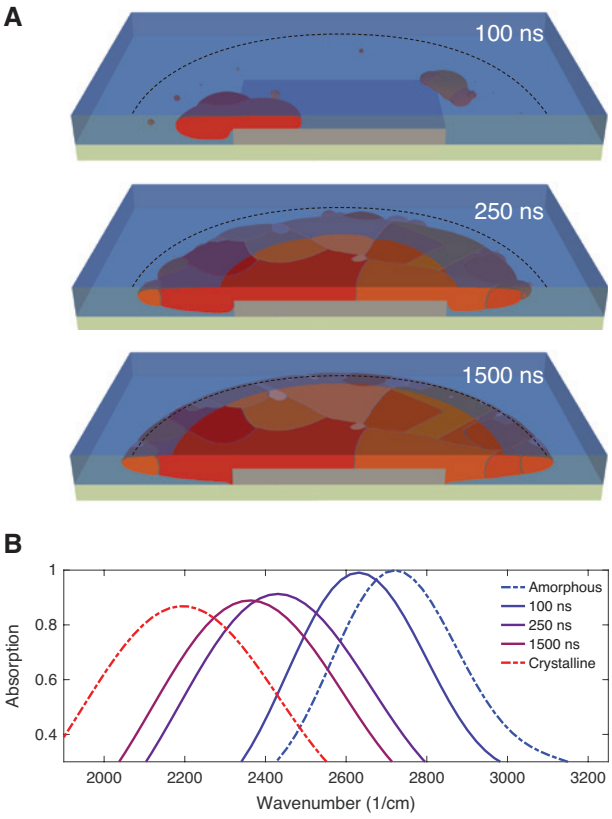

Figure 2: Multiphysics description of optical switching. (A) Snapshots of the crystallization state induced by a Gaussian beam after 100 ns, 150 ns and 1.5 µs. The buffer layer is shown in green. The square antenna is shown in gray. Blue semi-transparent volume represents the amorphous phase. Other colors code different crystalline phase grains. The superstrate layer is not shown for clarity. The dashed semicircle denotes the waist of the laser beam. (B) Absorption spectrum after 100 ns, 150 ns and 1.5 µs corresponding to the crystallization states from (A). Dashed-dotted lines correspond to the spectrum of the perfect absorber for a completely amorphous (blue) and crystalline (red) GST layer.

the periphery of the beam. The fastest growing nuclei are located near the beam center. This is related to the temperature distribution in the illuminated area, with the temperature dropping from the center towards its edge (SI). The maximum nucleation rate of GST is at around 580 K, while the maximum of the growth velocity is at around 790 K (SI). This naturally promotes nucleation (growth) in the periphery (center) of the illuminated area. After 250 ns, a large connected crystallized disk with a complex cross-section has formed around the antenna. The disk touches the upper surface of the GST layer (seen as a circle with brighter colors in Figure 2A), but not its bottom surface. After 1.5 µs, the crystallized volume finally touches the bottom surface of the GST layer just near the nano-antenna edges. At later times, the crystallized volume slowly grows with insignificant change of its shape.

The change of the absorption spectra during optically induced tuning is shown in Figure 2B. The spectra are calculated for an array assuming identically switched unit cells. It can be seen that with increasing illumination time the spectral position of the absorption band shifts from the fully amorphous towards the fully crystalline response. After 1.5 µs, a shift of 365 cm^{-1} is reached which is approximately 70% of the maximum achievable shift. In Figure 3 the spectral position of the absorption maximum as a function of the switching duration is shown. During the first 50 ns no visible spectral shift can be detected. At that time, there is no significant crystallized volume near the nano-antenna. After the first 75 ns, the spectral shift changes very rapidly for the next 125 ns. During this time, around 50% of the maximum achievable shift is reached. This fast switching regime is followed by a much slower one. Another 1000 ns are required to reach in total 70% of the maximum shift. A larger total shift can still be achieved for longer illumination times, but the timescale for full switching is significantly larger than considered here. Since nucleation is a statistical process, different simulation runs will lead to a different spatial distribution of grains. However, accompanying differences in the spectral response between different runs are small.

The character of the temporal evolution of the resonance tuning is due to an interplay of the antenna geometry, the evolution of the distribution of the crystallized volume and temperature field. In Figure 4 the temperature evolution at two depths in the GST layer (10 and 30 nm from the top surface of the GST layer) in the center of the illuminated area is shown. The temperature at the smaller depth stays considerably higher for all times. The temperature increases quickly from a room temperature of 297 K and saturates after around 30 ns. During this time first nuclei start to form (top panel 1) and no significant resonance shift is expected. Since the temperature in the periphery of the beam is more favorable for the nucleation events, the first nuclei are formed close to the nano-antenna perimeter. Such location of the crystallized volume is also beneficial for the resonance tuning due to an optimal overlap of the nano-antenna field with the volumes of high refractive index. As the fraction of the crystallized material grows between 50 and 120 ns (top panel 2), a major shift of the absorption band is observed. This process is accompanied by the temperature increase due to the additional optical loss in the crystalline phase of GST. At around 125 ns, the temperature starts to drop again, rapidly reaching a steady-state temperature. The first crystalline grains begin to reach the center of the illumination area (top panel 3) at that time, leading to a better heat transport away from the center due to the higher thermal conductivity of crystalline GST. This effect is significantly more pronounced than the increase of the absorption. The highest reached steady-state temperature (approximately 700 K) is considerably lower than the temperature of the maximum growth velocity (close to 800 K). This results in a considerable slowing down of the resonance tuning after the first 200 ns. A complex interplay of the optical absorption and the heat transfer during the

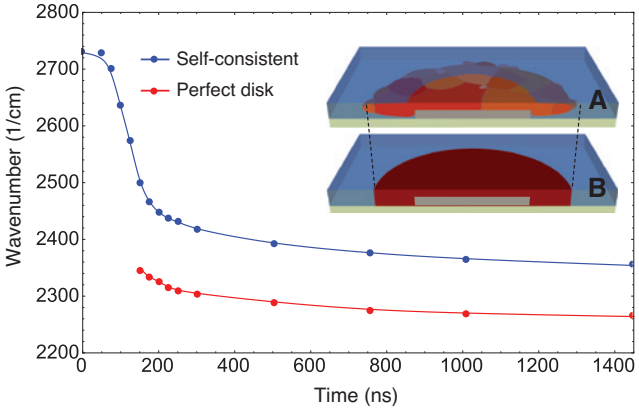

Figure 3: Comparison between idealized and multiphysics descriptions.
Position of the absorption maximum as a function of the time for the multiphysics model (A) and the corresponding idealized cylindrical crystallized volume model (B). Points are the results of the calculations, and lines are a guide for the eye. The inset illustrates the connection between two models (at time 250 ns). The buffer layer is shown in green. The square antenna is shown in gray. Blue semi-transparent volume represents the amorphous phase. Other colors code different crystalline phase grains.

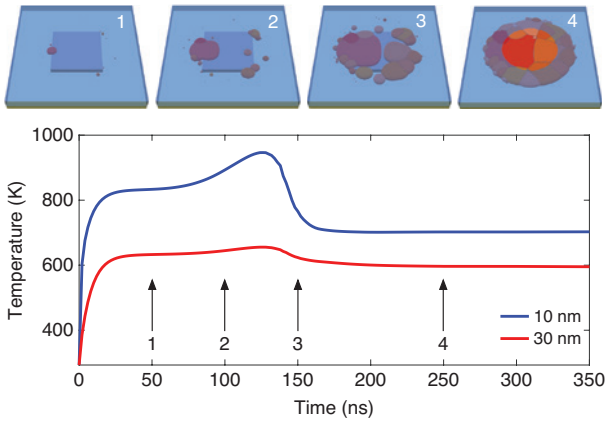

Figure 4: Crystalization steps and temperature evolution.
Temperature evolution at two depths in the GST layer (10 and 30 nm from the top surface of the GST layer) in the center of the illuminated area. Top panels 1–4 show the distribution of the crystalline phase at the marked times. The buffer layer is shown in green. The square antenna is shown in gray. Blue semi-transparent volume represents the amorphous phase. Other colors code different crystalline phase grains.

phase transition influences in a non-trivial manner both the tuning rate and maximal achievable resonance shift. This stresses the importance of a careful thermal and phase transition design of PCM-based MSs. The exact time at which the temperature changes occur can vary slightly between simulation runs due to statistical nature of the nucleation.

Full three-dimensional local information on the crystallized volume is not available in experiments, if non-destructive analysis is used [29]. Using optical inspection from above, only information on the spot area can be gained. In Figure 3 we compare the actual spectral shift (blue curve) with the shift, which would be obtained from a cylindrical crystallized volume with a height of the complete PCM layer thickness and a diameter determined from the inspection of the sample from above (red curve). Before 150 ns, the simulated crystallized volume does not form a coherent circular shape (Figure 4), so it is impossible to correlate two models. For later times, the cylinder approximation significantly overestimates the absorption peak shift. The differences decrease marginally for later time reaching 90 cm^{-1} at 1.5 µs, which corresponds to a 20% overestimated total shift. Though the effective diameter of the switched volume is considerably larger than the antenna dimensions, in the direct vicinity of the antenna, perimeter PCM material is not yet crystallized through full GST thickness. This results in the smaller resonance shift, as expected. The observation stresses the importance of detailed knowledge about the switched volume shape and size for an adequate description of the spectral properties of PCM-based MSs.

3 Conclusions

Recent experimental progress in the local optical addressing of PCM-based MSs promises to revolutionize (re-)programmable adaptive flat photonics. Novel possibilities open new challenges, one of which is a necessity to understand and be able to predict the phase transition behavior at the scale of a single meta-atom. Here, we reported on the development of a multiphysics tool which enables a self-consistent description of transient electromagnetic, heat transfer and phase transition phenomena at the meta-atom scale. We demonstrate, using an MS perfect absorber as an example, that a detailed understanding of the crystallization both in space and time is essential to correctly explain and predict the behavior of a PCM-based MS. The reported model is not limited to $Ge_2Sb_2Te_5$, but can be adapted for any PCM. It can readily be applied not only to optically but also electrically controlled PCM systems. The multiphysics model can also be further extended to include self-consistent description of re-amorphization and effects of elastic deformation and grain interaction. A self-consistent multiphysics description of the phase transition in PMC-based MSs enables improved, purposeful design of programmable adaptive MSs.

Acknowledgments: The authors are thankful to Andreas Heßler and Thomas Taubner for useful discussions and careful reading of the manuscript. DNC acknowledges a partial support by the DFG through the Heisenberg Fellowship (CH 407/7-2, Funder Id: http://dx.doi.org/10.13039/501100001659).

References

[1] Yu N, Capasso F. Flat optics with designer metasurfaces. Nat Mater 2014;3:139–50.
[2] Kildishev AV, Boltasseva A, Shalaev VM. Planar photonics with metasurfaces. Science 2013;339:1232009.
[3] Genevet P, Capasso F, Aieta F, Khorasaninejad M, Devlin R. Recent advances in planar optics: from plasmonic to dielectric metasurfaces. Optica 2017;4:139–52.
[4] Jahani S, Jacob Z. All-dielectric metamaterials. Nat Nanotechnol 2016;11:23–36.
[5] Xiao S, Chettiar UK, Kildishev AV, Drachev V, Khoo ICC, Shalaev VM. Tunable magnetic response of metamaterials. Appl Phys Lett 2009;95:033115.
[6] Decker M, Kremers C, Minovich A, et al. Electro-optical switching by liquid-crystal controlled metasurfaces. Opt Express 2013;21:8879.
[7] Buchnev O, Podoliak N, Kaczmarek M, Zheludev NI, Fedotov VA. Electrically controlled nanostructured metasurface loaded with liquid crystal: toward multifunctional photonic switch. Adv Opt Mater 2015;3:674–9.
[8] Colburn S, Zhan A, Majumdar A. Varifocal zoom imaging with large area focal length adjustable metalenses. Optica 2018;5:825.
[9] Arbabi E, Arbabi A, Kamali SM, Horie Y, Faraji-Dana MS, Faraon A. MEMS-tunable dielectric metasurface lens. Nat Commun 2018;9:812.
[10] Ju L, Geng B, Horng J, et al. Graphene plasmonics for tunable terahertz metamaterials. Nat Nanotechnol 2011;6:630–4.
[11] Sherrott MC, Hon PW, Fountaine KT, et al. Experimental demonstration of >230° phase modulation in gate-tunable graphene-gold reconfigurable mid-infrared metasurfaces. Nano Lett 2017;17:3027–34.
[12] Zhao H, Zhang R, Chorsi HT, et al. Gate-tunable metafi absorber based on indium silicon oxide. Nanophotonics 2019;8:1803–10.
[13] Miao X, Passmore B, Gin A, et al. Doping tunable resonance: toward electrically tunable mid-infrared metamaterials. Appl Phys Lett 2010;96:101111.
[14] Dicken MJ, Aydin K, Pryce IM, et al. Frequency tunable near-infrared metamaterials based on VO_2 phase transition. Opt Express 2009;17:18330–9.

[15] Chen H-T, Taylor AJ, MacDonald KF, Yu N. A review of metasurfaces: physics and applications. Rep Prog Phys 2016;79:076401.
[16] Li A, Singh S, Sievenpiper D. Metasurfaces and their applications. Nanophotonics 2018;7:989–1011.
[17] Raoux S, Welnic W, Ielmini D. Phase change materials and their application to nonvolatile memories. Chem Rev 2009;110:240–67.
[18] Boybat I, Le Gallo M, Nandakumar SR, et al. Neuromorphic computing with multi-memristive synapses. Nat Commun 2018;9:1–12.
[19] Kremers S. Optische Eigenschaften von Phasenwechselmaterialien fu¨r zuku¨nftige optis-che und elektronische Speicheranwendungen. Ph.D. thesis, RWTH Aachen University, 2009.
[20] Shportko K, Kremers S, Woda M, Lencer D, Robertson J, Wuttig M. Resonant bonding in crystalline phase-change materials. Nat Mater 2008;7:653–8.
[21] Wuttig M, Bhaskaran H, Taubner T. Phase-change materials for non-volatile photonic applications. Nat Photon 2017;11:465–76.
[22] Hail CU, Michel A-KU, Poulikakos D, Eghlidi H. Optical metasurfaces: evolving from passive to adaptive. Adv Opt Mater 2019;7:1801786.
[23] Ding F, Yang Y, Bozhevolnyi SI. Dynamic metasurfaces using phase-change chalcogenides. Adv Opt Mater 2019;7:1801709.
[24] Carrillo SGC, Trimby L, Au YY, et al. A nonvolatile phase-change meta-material color display. Adv Opt Mater 2019;7:1801782.
[25] Michel A-KU, Chigrin DN, Maß TWW, et al. Using low-loss phase-change materials for mid-infrared antenna resonance tuning. Nano Lett 2013;3:3470–5.
[26] Hosseini P, Wright CD, Bhaskaran H. An optoelectronic framework enabled by low-dimensional phase-change films. Nature 2014;511:206–11.
[27] Michel AU, Zalden P, Chigrin DN, Wuttig M, Lindenberg AM, Taubner T. Reversible optical switching of infrared antenna resonances with ultrathin phase-change layers using femtosecond laser pulses. ACS Photon 2014;1:833–9.
[28] Dong W, Liu H, Behera JK, et al. Wide bandgap phase change material tuned visible photonics. Adv Funct Mater 2019;29:1–9.
[29] Michel AU, Heßler A, Meyer S, et al. Advanced optical programming of individual meta-atoms beyond the effective medium approach. Adv Mater 2019;31:1901033.
[30] Wang Q, Rogers ET, Gholipour B, et al. Optically reconfigurable metasurfaces and photonic devices based on phase change materials. Nat Photon 2016;10:60–5.
[31] Li P, Yang X, Maß TWW, et al. Reversible optical switching of highly confined phonon-polaritons with an ultrathin phase-change material. Nat Mater 2016;15:870–5.
[32] Lee TH, Elliott SR. Ab initio computer simulation of the early stages of crystallization: application to Ge2Sb2Te5 phase-change materials. Phys Rev Lett 2011; 107:145702.
[33] Avrami M. Kinetics of phase change. J Chem Phys 1939;7: 1103–12.
[34] Johnson WA, Mehl RF. Reaction kinetics in processes of nucleation and growth. Trans Am Inst Mining Met Eng 1939;135:416–42.
[35] Avrami M. Kinetics of phase change. I: General theory. J Chem Phys 1939;7:1103–12.
[36] Avrami M. Kinetics of phase change. II: Transformation – time relations for random distribution of nuclei. J Chem Phys 1940;8:212–24.
[37] Avrami M. Kinetics of phase change. III: Granulation, phase change, and microstructure. J Chem Phys 1941;9:177–84.
[38] Senkader S, Wright CD. Models for phase-change of Ge2Sb2Te5 in optical and electrical memory devices. J Appl Phys 2004;95:504–11.
[39] Ashwin P, Patnaik BS, Wright CD. Fast simulation of phase-change processes in chalcogenide alloys using a Gillespie-type cellular automata approach. J Appl Phys 2008; 104:1–8.
[40] Kwon Y, Kang DH, Lee KH, Park YK, Chung CH. Analysis of intrinsic variation of data retention in phase-change memory using phase-field method. IEEE Electr Device Lett 2013;34:411–3.
[41] Iwamatsu M. Direct numerical simulation of homogeneous nucleation and growth in a phase-field model using cell dynamics method. J Chem Phys 2008;128:084504.
[42] Tabatabaei F, Boussinot G, Spatschek R, Brener EA, Apel M. Phase field modeling of rapid crystallization in the phase-change material AIST. J Appl Phys 2017;122:045108.
[43] Moelans N, Blanpain B, Wollants P. An introduction to phase-field modeling of microstructure evolution. Calphad 2008;32:268–94.
[44] Emmerich H, Lo¨wen H, Wittkowski R, et al. Phase-field-crystal models for condensed matter dynamics on atomic length and diff e time scales: an overview. Adv Phys 2012;61:665–743.
[45] Allen SM, Cahn JW. A microscopic theory for antiphase boundary motion and its application to antiphase domain coarsening. Acta Metall Mater 1979;27:1085–95.
[46] Cahn JW, Hilliard JE. Free energy of a nonuniform system. I: Interfacial free energy. J Chem Phys 1958;28:258–67.
[47] Wilson HA. On the velocity of solidification and viscosity of supercooled liquids. Phil Mag 1900;50:238.
[48] Frenkel J. On the electric and photoelectric properties of contacts between a metal and a semi-conductor. Phys Z Sowjetunion 1932;1:498.
[49] Thompson CV, Spaepen F. On the approximation of the free energy change on crystallization. Acta Metall Mater 1979;27:1855–9.
[50] Simmons J, Shen C, Wang Y. Phase field modeling of simultaneous nucleation and growth by explicitly incorporating nucleation events. Script Mater 2000;43:935–42.
[51] Kelton KF. Crystal nucleation in liquids and glasses. In: Ehrenreich H, Turnbull D, eds. Vol. 45, Solid state physics. Cambridge, MA, USA, Academic Press, 1991:75–177.
[52] Wu D, Gránásy L, Spaepen F. Nucleation and the solid–liquid interfacial free energy. MRS Bull 2004;29:945–50.
[53] Weidenhof V, Friedrich I, Ziegler S, Wuttig M. Laser induced crystallization of amorphous Ge2Sb2Te5 films. J Appl Phys 2001;89:3168–76.
[54] Tittl A, Michel A-K, Schäferling M, et al. Plasmonic absorbers: a switchable mid-infrared plasmonic perfect absorber with multispectral thermal imaging capability. Adv Mater 2015;27: 4597–603.
[55] Lyeo HK, Cahill DG, Lee BS, et al. Thermal conductivity of phase-change material Ge2Sb2Te5. Appl Phys Lett 2006;89:2006–9.

Supplementary Material: The online version of this article offers supplementary material (https://doi.org/10.1515/nanoph-2019-0458).